

NON-EQUILIBRIUM IONIZATION STATE OF WARM–HOT INTERGALACTIC MEDIUM

Kohji YOSHIKAWA

Department of Physics, School of Science, University of Tokyo, Tokyo 113-0033, Japan

kohji@utap.phys.s.u-tokyo.ac.jp

and

Shin SASAKI

Department of Physics, Tokyo Metropolitan University,

1-1 Minami-Osawa, Hachioji, Tokyo 192-0397, Japan

(Received ; accepted)

Abstract

Time evolution of the ionization state of metals in the cosmic baryons is investigated in a cosmological context without the assumption of ionization equilibrium. We find that a significant fraction of ionized oxygen (O VII and O VIII) in the warm-hot intergalactic medium (WHIM) is not in the ionization equilibrium state at a redshift of $z \simeq 0$. We also investigate the effect on the detectability and observables of WHIM as a consequence of such deviation from ionization equilibrium. It is found that the detectability of WHIM is not altered very much both through its emission and absorption signatures, but line ratios between O VII and O VIII are significantly different from those in the ionization equilibrium state.

Key words: cosmology: miscellaneous — X-rays: general — methods: numerical

1. INTRODUCTION

After Fukugita, Hogan, & Peebles (1998) first pointed out the importance of studying the cosmic baryon budget, it is now widely accepted that only less than half of the cosmic baryons in the present universe have been detected, and the remaining portion, “the missing baryon”, has evaded the direct detection so far. Numerical simulations by Cen & Ostriker (1999) suggest that approximately 30 to 50 % of the cosmic baryons at $z = 0$ are in the form of the diffuse intergalactic medium with temperature of $10^5 \text{ K} < T < 10^7 \text{ K}$ which is called warm-hot intergalactic medium (WHIM), and subsequent numerical simulations (e.g., Davé et al. 2001) with different numerical schemes and resolutions also support this picture consistently. Based on these numerical predictions, many observational efforts have been made to reveal the existence

of WHIM.

Since the observational signature of WHIM is very weak, the detection of WHIM is observationally quite challenging and first proposed through its metal absorption features in the bright background beacons such as QSOs and blazars (Hellsten, Gnedin & Miralda-Escude 1998; Perna & Loeb 1998; Fang & Canizares 2000; Cen et al. 2001; Fang & Bryan 2001). After the first detection of O VI absorption lines in the spectra of a bright QSO H1821+643 by Tripp, Savage, & Jenkins (2000) and Tripp et al. (2001), number of detections are reported through absorption features of O VI, O VII, O VIII and Ne IX ions (Nicastro et al. 2002; Fang et al. 2002; Mathur et al. 2003; Fujimoto et al. 2004), but they are rather tentative. Only recently, the detection with sufficient signal-to-noise ratio is reported by Nicastro et al. (2005a) and Nicastro et al. (2005b) in which absorption signatures of WHIM are found at two redshift in the spectra of the blazer Mrk421 during its two outburst phases. Future proposed missions such as *Constellation-X* and *XEUS* are expected to detect numerous WHIM absorbers. Detection of WHIM absorption in the spectra of afterglows of gamma-ray bursts (GRBs) are also proposed by Elvis & Fiore (2003) and Elvis, Nicastro & Fiore (2004) using a dedicated mission such as *Pharos*. Kawahara et al. (2005) investigate the feasibility of such detections in a realistic manner based on cosmological hydrodynamic simulations. As an alternative strategy, several tentative detections of WHIM through its metal line emission are claimed by Kaastra et al. (2003), and Finoguenov, Briel, & Henry (2003) using *XMM-Newton* satellite. However, these detections are not significant enough to exclude the possibility that the observed emission lines are the Galactic ones because of the limited energy resolution ($\simeq 80\text{eV}$) of the current X-ray detectors. Recently, Yoshikawa et al. (2003), Yoshikawa et al. (2004), and Fang et al. (2005) show that future X-ray missions equipped with a high energy resolution spectrograph such as *DIOS* (Diffuse Intergalactic Oxygen Surveyor) and *MBE* (Missing Baryon Explorer) can detect the line emission of WHIM in a convincing manner. Future X-ray observations of WHIM through its emission and absorption features are expected to unveil the physical properties of WHIM beyond its existence.

So far, most of theoretical and observational studies on WHIM assume that the cosmic baryons are in their ionization equilibrium under a given physical condition, irrespective of their thermal history. However, as shown in this paper, some portion of the cosmic baryons is expected to deviate from ionization equilibrium depending on its thermal history, since the timescales of ionization and recombination processes can be comparable or even longer than the age of the universe in a low density plasma such as WHIM. In this paper, we focus on the non-equilibrium ionization state of metals in WHIM. Since ionized metals such as O VI–VIII and Ne IX are supposed to be good tracers of WHIM, the ionization state of such metals and their deviation from the ionization equilibrium state are of great importance in studying the detectability of WHIM and probing its physical condition. By relaxing the assumption that the cosmic baryons are in the ionization equilibrium, we follow the time evolution of the ionization

state of metals as well as hydrogen and helium in cosmological hydrodynamic simulations, and investigate to what extent the effect of the non-equilibrium ionization state affects the detectability and observational features of WHIM.

The rest of the paper is organized as follows. The importance of non-equilibrium treatment of ionization balance in WHIM is described in section 2. In addition, technical details in computing time evolution of ionization fractions of ions are also shown in section 2. In section 3, we consider a simple model of thermal histories of the cosmic baryons, and investigate the non-equilibrium ionization state of oxygen ions and their deviations from the ionization equilibrium state to understand general properties of the ionization history of oxygen in the cosmic baryons. The non-equilibrium ionization balance in the cosmological hydrodynamic simulation is shown in section 4, and the effect of the non-equilibrium ionization state on the detectability and observational features of WHIM is investigated in section 5. Finally, in section 6, we summarize our conclusion and discuss other important physical processes which may also affect the ionization state of WHIM. Throughout this paper, unless otherwise stated, we adopt a spatially flat cosmology with $\Omega_m = 0.3$, $\Omega_\Lambda = 0.7$, $\Omega_b = 0.04$, and $h = 0.7$, where Ω_m is the density parameter, Ω_Λ the dimensionless cosmological constant, Ω_b the baryon density parameter, and h the hubble constant in units of $100\text{km s}^{-1}\text{Mpc}^{-1}$.

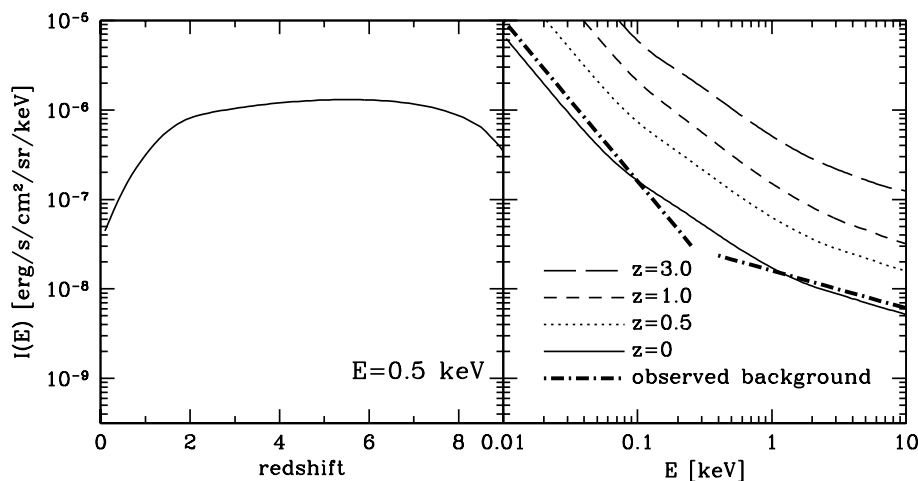


Fig. 1. Redshift dependence of the cosmic UV and X-ray background radiation at photon energy of 0.5 keV (left panel) and its spectrum at redshift $z = 0, 0.5, 1$, and 3 (right panel). In the right panel, we also show the observed background spectra in UV and X-ray bands obtained by Shull et al. (1999) and Miyaji et al. (1998), respectively.

2. IONIZATION BALANCE

The time evolution of ionization balance in collisionally- and photo-ionized plasmas can be described by

$$\frac{df_j}{dt} = \sum_{k=1}^{j-1} S_{j-k,k} f_k - \sum_{i=j+1}^{Z+1} S_{i-j,j} f_j - \alpha_j f_j + \alpha_{j+1} f_{j+1}, \quad (1)$$

where j is the index of a particular ionization stage considered, Z the atomic number, f_j the ionization fraction of an ion j . $S_{i,j}$ denotes the ionization rate for an ion j with the ejection of i electrons, and α_j is the recombination rate of ion j . As ionization processes, collisional, Auger, charge-transfer and photo-ionizations are taken into account. Recombination processes are composed of radiative and dielectric recombinations. The ionization equilibrium state, f_j^{eq} , can be obtained by solving

$$0 = \sum_{k=1}^{j-1} S_{j-k,k} f_k^{\text{eq}} - \sum_{i=j+1}^{Z+1} S_{i-j,j} f_j^{\text{eq}} - \alpha_j f_j^{\text{eq}} + \alpha_{j+1} f_{j+1}^{\text{eq}}. \quad (2)$$

Ionization and recombination rates adopted in this paper are calculated by utilizing the SPEX¹ ver 1.10 software package.

As a source of photoionization, we adopt UV and X-ray background radiation calculated using the CUBA code² (Haardt & Madau 2001) throughout this paper. The spectra and redshift evolution of the adopted background radiation are shown in figure 1. It should be noted that the intensity of the background radiation rapidly drops at redshift $z < 2$, while the overall spectral shapes do not change so much. In the right panel, we overlay the observed UV and X-ray background radiation estimated by Shull et al. (1999) and Miyaji et al. (1998), respectively, for comparison. It can be seen that the spectrum of adopted background radiation at $z = 0$ is consistent with the observed ones within a factor of two. Although ionization fractions of ions in the collisional ionization equilibrium entirely depend on gas temperature, they depend on gas density as well as gas temperature under the presence of photoionizing background radiation, and the effect of photoionization by the UV and X-ray background is important in a low density and low temperature plasma. Figure 2 shows the ionization fractions of O VI, O VII and O VIII ions in collisional ionization equilibrium (i.e. no background radiation) and those in ionization equilibrium under the presence of the UV and X-ray background at $z = 0$. It is obvious that the effect of photoionization is quite important at a typical temperature range of WHIM ($10^5 \text{ K} < T < 10^7 \text{ K}$) and that it increases the ionization fractions of ionized oxygen in a lower density regime.

According to equation (1), the timescales of ionization and recombination for an ion j , τ_{ion} and τ_{rec} respectively, can be estimated by

¹ <http://www.sron.nl/divisions/hea/spex/>

² <http://pitto.mib.infn.it/~haardt/cosmology.html>

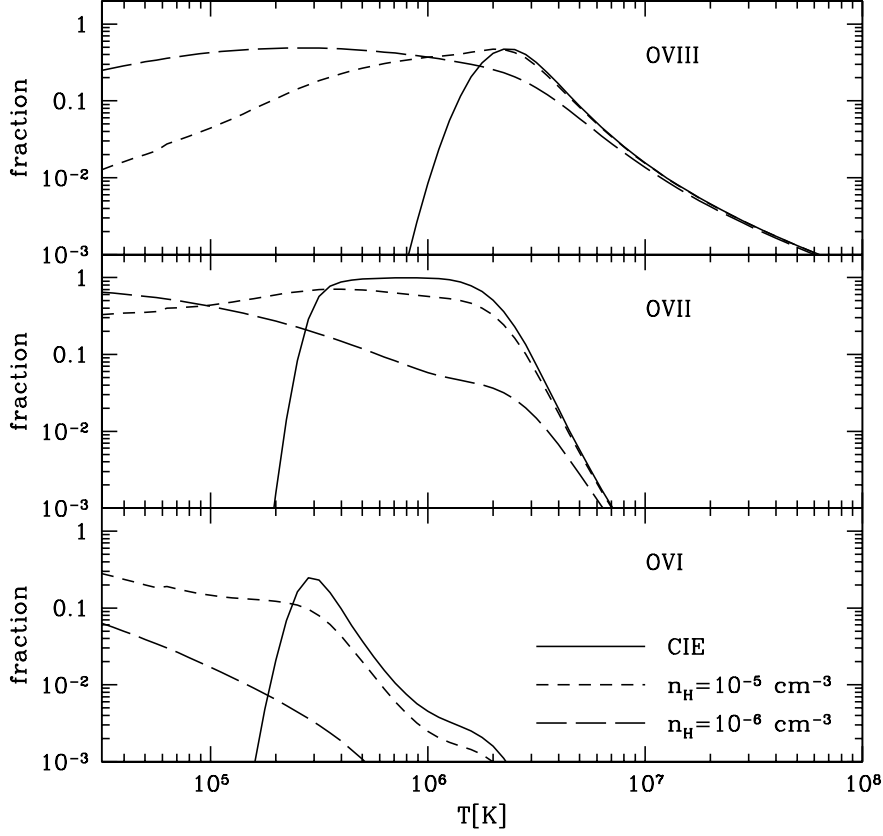


Fig. 2. Ionization fractions of O VI, O VII and O VIII in ionization equilibrium as a function of temperature for the low density plasma with $n_{\text{H}} = 10^{-5}$ and 10^{-6} cm^{-3} under the presence of photoionizing background radiation at a redshift of $z = 0$. Ionization fractions in collisional ionization equilibrium are also shown for the comparison.

$$\tau_{\text{ion}} = \left(\sum_{i=j+1}^{Z+1} S_{i-j,j} \right)^{-1} \quad (3)$$

and

$$\tau_{\text{rec}} = \alpha_j^{-1}. \quad (4)$$

Figure 3 shows temperature dependence of τ_{ion} and τ_{rec} of O VI, O VII and O VIII ions for hydrogen number density of $n_{\text{H}} = 10^{-5}$ and 10^{-6} cm^{-3} under the presence of the photoionizing background radiation at a redshift of $z = 0$. In a temperature range $T \gtrsim 10^6 \text{ K}$, the recombination timescales are longer than the ionization timescales, and are comparable to or even longer than the hubble time, $H_0^{-1} (\simeq 13 \text{ Gyr})$, where $H_0 = 100h \text{ km s}^{-1} \text{ Mpc}^{-1}$ is the hubble constant. In a lower temperature regime with $T \lesssim 10^6 \text{ K}$, the recombination timescales are still comparable to the hubble time for hydrogen number density of $n_{\text{H}} = 10^{-6} \text{ cm}^{-3}$. The ionization timescales in

the lowest temperature range ($\simeq 10^5$ K) are determined by the intensity of the UV and X-ray background radiation. It can be seen that the ionization timescales of O VII and O VIII ions are also comparable to the hubble time at a temperature of $T \lesssim 10^6$ K. Actually, these behaviors of ionization and recombination timescales are also the case for hydrogen- and helium-like ions of other metal such as carbon and nitrogen. Considering these facts, one can easily expect that the ionization balance is not in the equilibrium state in a low density plasma like WHIM. Therefore, for proper treatment of ionization balance in WHIM, we have to follow the time evolution of ionization fractions by directly integrating equation (1).

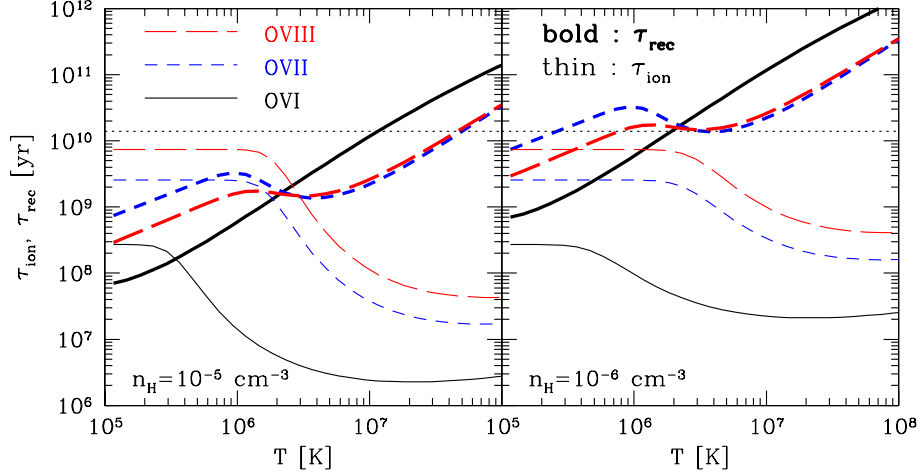


Fig. 3. Timescales of ionization and recombination for O VI, O VII and O VIII ions in hydrogen number density of $n_H = 10^{-5} \text{ cm}^{-3}$ (left) and 10^{-6} cm^{-3} (right) under the presence of UV and X-ray background radiation at a redshift of $z = 0$. Horizontal dotted lines indicate the hubble time H_0^{-1} ($\simeq 13 \text{ Gyr}$).

Since the timescales for the ionization and recombination differ by many order of magnitude depending on ionic species and ionization stages, equation (1) is a stiff set of differential equations. In numerically solving a stiff set of equations, explicit integration schemes are unstable unless unreasonably small timestep is taken, which leads to prohibitively expensive computations. Therefore, implicit schemes are required to numerically integrate equation (1). In this paper, we adopt a backward difference formula (BDF), which is also adopted in Anninos et al. (1997) for solving chemical reactions of atomic and molecular hydrogen in the primordial universe. In the BDF, ionization fractions of all ionic species are sequentially updated in the order of increasing ionization states rather than being updated simultaneously, and the source terms contributed by the ionization from and recombination to the lower states are evaluated at the advanced timestep. The discretization of equation (1) can be written as

$$f_j^{t+\Delta t} = \frac{\left(\sum_{k=1}^{j-1} S_{j-k,k} f_k^{t+\Delta t} + \alpha_{j+1} f_{j+1}^t \right) \Delta t + f_j^t}{1 + \left(\sum_{i=j+1}^{Z+1} S_{i-j,j} + \alpha_j \right) \Delta t}. \quad (5)$$

We confirm that this scheme is stable and as accurate as the eigenvalue decomposition scheme by

Kaasta & Jansen (1993) adopted for solving the non-equilibrium ionization state in supernova remnants, but our scheme is found to be computationally less expensive. In this paper, we simultaneously solve the time evolution of ionization fractions of H, He, C, N, O, Ne, Mg, Si, and Fe, but we focus on only the ionization states of oxygen.

Throughout this paper, we assume spatially uniform and time independent metallicity of $Z = 0.1Z_{\odot}$, where Z_{\odot} denotes the solar abundance. Note that the metallicity Z is very insensitive to the resulting non-equilibrium ionization state as long as $Z \ll 1$. Of course, in reality, metals in intergalactic medium are ejected from galaxies through the feedback of star formation activities, and thus the distribution of metals is inhomogeneous and time dependent. Actually, for a fully consistent treatment, such feedback effect must be included in the rhs of equation (1) as a source term. In this paper, however, since we are interested in the non-equilibrium ionization state that arise along the thermal histories of baryons in a context of cosmological structure formation, we adopt such an assumption and believe that it is acceptable for qualitative studies of ionization states of WHIM.

3. SIMPLE MODELS

In this section, we explore the general behaviors of the non-equilibrium ionization state using simple thermal histories of the cosmic baryons. Here, we consider a series of thermal histories depicted in figure 4, in which baryonic matter has hydrogen number density $n_{\text{H},0}(1+z_i)^3$ and temperature T_i at an initial redshift of $z_i = 10$, keeps its comoving density and temperature constant before increasing its density and temperature to $n_{\text{H}} = n_{\text{H},0}(1+\delta_s)$ and $T = T_s$, respectively, by experiencing shock heating at redshift $z = z_s$, and keeps the postshock thermal state till $z = 0$. A physical scenario we have in mind is that the baryonic matter is diluted according to the cosmological expansion until it experiences the cosmological shock heating, and that it gets quasi-virialized inside collapsed halos or filamentary structures after the shock heating. Here $n_{\text{H},0}$ is the present-day hydrogen number density, and we set the initial temperature to $T_i = 5 \times 10^3 \text{ K}$. Therefore, these thermal histories can be parametrized by three parameters, the postshock overdensity δ_s , postshock temperature T_s , and the redshift of shock heating z_s . In a cosmological model adopted in this paper, we have $n_{\text{H},0} = 2.2 \times 10^{-7} \text{ cm}^{-3}$. We assume the UV and X-ray background radiation described in the previous section as a photoionization source, irrespective of the adopted thermal histories.

Actually, the thermal history of the cosmic baryon in a cosmological hydrodynamic simulation is fairly well represented by this simple model. Figure 5 shows the time evolution of temperature and hydrogen number density of gas particles from a cosmological hydrodynamic simulation presented in section 4. In both panels, time evolutions of five randomly selected gas particles inside a filamentary structure at $z = 0$ are shown. One can see that each gas particle have nearly constant temperature and physical density proportional to $(1+z)^{-3}$ before it experiences the first shock heating. After the first shock heating, although thermal histories

of gas particles in the simulation is not so simple as that presented in figure 4, it can be a viable model for qualitative description of the thermal history of the cosmic baryon since the timescales for temporal variations in density and temperature are much shorter than τ_{ion} and τ_{rec} of oxygen ions (O VI, O VII and O VIII). It should be noted that, in figure 5, we can see that some particles experience multiple shocks in a sufficiently short timescale compared with τ_{ion} and τ_{rec} , and increase their postshock density by a factor larger than 4, the value in the strong shock limit. Therefore, we allow the density jump at $z = z_s$ to be greater than a factor of 4 in order to bracket the plausible range of the thermal histories of the cosmic baryons.

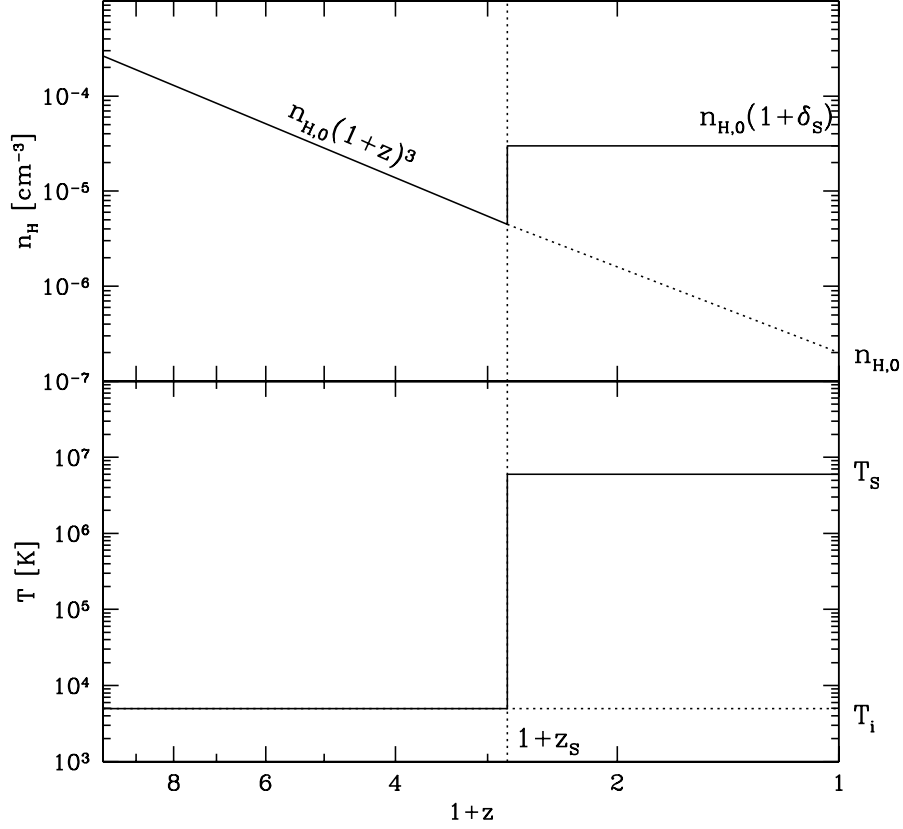


Fig. 4. Time evolution of density and temperature of baryons for the model calculations. We have three free parameters δ_s , T_s and z_s . (see text for detail.)

At the initial redshift $z_i = 10$, we assume that all baryons are in the ionization equilibrium state. This assumption can be justified by the fact that physical gas density is so high at such a high redshift that ionization equilibrium can be quickly realized. Equation (1) is integrated along the thermal histories described above till $z = 0$ for a given set of parameters δ_s , T_s , and z_s . Figure 6 shows the ratios of the resulting ionization fractions at $z = 0$ for thermal histories with $z_s = 1.0$ relative to those in the ionization equilibrium state, f_j/f_j^{eq} , for O VI, O VII, O VIII

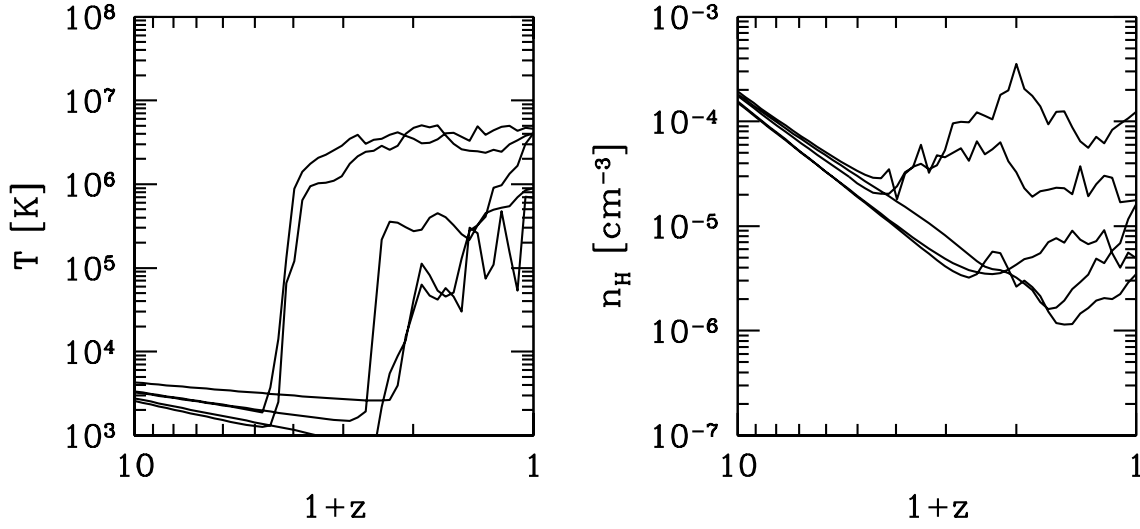


Fig. 5. Time evolution of temperature (left panel) and hydrogen number density (right panel) of gas particles in a cosmological hydrodynamic simulation presented in section 4. See section 4 for details of the simulation.

and O IX on a $(1 + \delta_s) - T_s$ plane. White contour lines are separated by a factor of 1.1 in ratios of ionization fractions, f_j/f_j^{eq} , where the bold lines are contours for $f_j/f_j^{\text{eq}} = 1$. Black contours with numeric labels indicate the ionization fractions in the ionization equilibrium state on $(1 + \delta_s) - T$ plane. One can see that, for O VI ion, the ratios of ionization fractions significantly deviate from unity only in the region where O VI fraction in the equilibrium state, $f_{\text{OVI}}^{\text{eq}}$, is negligible, and close to the equilibrium value in the region where $f_{\text{OVI}}^{\text{eq}}$ is higher than 0.1. This is because, as can be seen in figure 3, timescales for both of ionization and recombination of O VI ions are much shorter than the hubble time in the density and temperature ranges where $f_{\text{OVI}}^{\text{eq}}$ is significant. On the other hand, for O VII, O VIII and O IX, we have significant deviation from the ionization equilibrium state in those density and temperature ranges in which their ionization fractions are not negligible, especially at low density regions with $1 + \delta_s < 1.5$. Only the region with $1 + \delta_s > 10$ and $T_s > 10^{6.5}\text{K}$ is almost free from significant deviation from the ionization equilibrium state.

Figure 7 shows the time evolution of ionization fractions of O VII, O VIII and O IX for thermal histories with four sets of $1 + \delta_s$ and T_s marked in figure 6 (A, B, C and D) and $z_s = 1.0$. For all the thermal histories, ionization fractions of O VIII increase rapidly just after the shock heating, while those in the ionization equilibrium state are lower than the preshock ionization fractions. This is because the timescale for collisional ionization to O VIII ion is much shorter than that of recombination timescale. After taking their maximum values, O VIII fractions decrease toward the equilibrium fractions. Ionization to O IX ions slightly slower and is delayed compared with that to O VIII ions. Ionization fractions in the equilibrium state also change

in time because the intensity of the UV and X-ray background radiation is decreasing at a redshift $z \lesssim 2$. In the history A with $1 + \delta_s = 10$ and $T = 10^6$ K, O VIII and O IX fractions in the ionization equilibrium state are increasing and decreasing in time, respectively. In the non-equilibrium ionization state, however, the ionization fractions of these ions cannot catch up with the ionization equilibrium state because of slow recombination processes from O IX to O VIII. Therefore, it can be said that the decrease of the UV and X-ray background radiation at $z \lesssim 2$ is so rapid that it eventually enlarge the deviation from the ionization equilibrium state. The similar behavior can be also seen in the histories C and D. On the contrary, in the history B with higher density and temperature than A, the ionization equilibrium is achieved because ionization processes are dominated by collisional ionization and the decrease in UV and X-ray background intensity does not significantly change the equilibrium ionization fractions. Figures 8 and 9 are the same as figure 6 but for results with $z_s = 0.5$ and 0.1 , respectively. As is the case for the results with $z_s = 1.0$, we also have significant deviation from ionization equilibrium for O VII, O VIII and O IX ions, while O VI fractions are close to the ionization equilibrium states for the region where $f_{\text{OVI}}^{\text{eq}} > 0.1$. For $z_s = 0.5$ and 0.1 , fractions of O VII and O VIII are larger than the equilibrium fractions, while O IX ion is under-ionized in regions with $1 + \delta_s < 10$ and $T_s > 10^6$ K. These features can be understood by the same argument as the result for a history with $z_s = 1.0$ that the timescale for ionization to O VIII is much shorter than that of recombination from O VIII to O VII, and that ionization to O IX is slower than that to O VIII.

4. RESULTS IN COSMOLOGICAL SIMULATION

In this section, we compute the non-equilibrium ionization state for more realistic thermal histories of baryons obtained from a cosmological hydrodynamic simulation. The simulation data of Yoshikawa et al. (2003) is used in this paper, which is computed using a hybrid code of a Particle–Particle–Particle–Mesh (PPPM) poisson solver and smoothed particle hydrodynamics (SPH) scheme. The details of our code are described in Yoshikawa et al. (2001). We adopt a spatially flat Λ CDM universe with $\Omega_m = 0.3$, $\Omega_\Lambda = 0.7$, $\Omega_b = 0.015h^{-2}$, $\sigma_8 = 1.0$ and $h = 0.7$, where σ_8 is the r.m.s. density fluctuation smoothed over a scale of $8h^{-1}$ Mpc. We employ 128^3 particles each for dark matter and gas particles within a periodic simulation box of $75h^{-1}$ Mpc per side. Therefore, the mass of each dark matter and gas particle is $2.2 \times 10^{10} M_\odot$ and $2.4 \times 10^9 M_\odot$, respectively. The effect of radiative cooling is incorporated using the cooling rate for a metallicity of $[\text{Fe}/\text{H}] = -0.5$ by Sutherland & Dopita (1993). The effect of energy feedback from supernovae is ignored in our simulation.

The initial condition is setup at $z = 36$ and we have 51 outputs from $z = 9$ to $z = 0$ with an equal interval in $\ln(1 + z)$. For each gas particle, we integrate equation (1) till $z = 0$ using the BDF described by equation (5) using its thermal history, or more specifically, a history of its density and temperature. As an initial condition of equation (1), the output at $z = 9$ is adopted. As in the simple model, it is assumed that all baryons are in the ionization equilibrium state

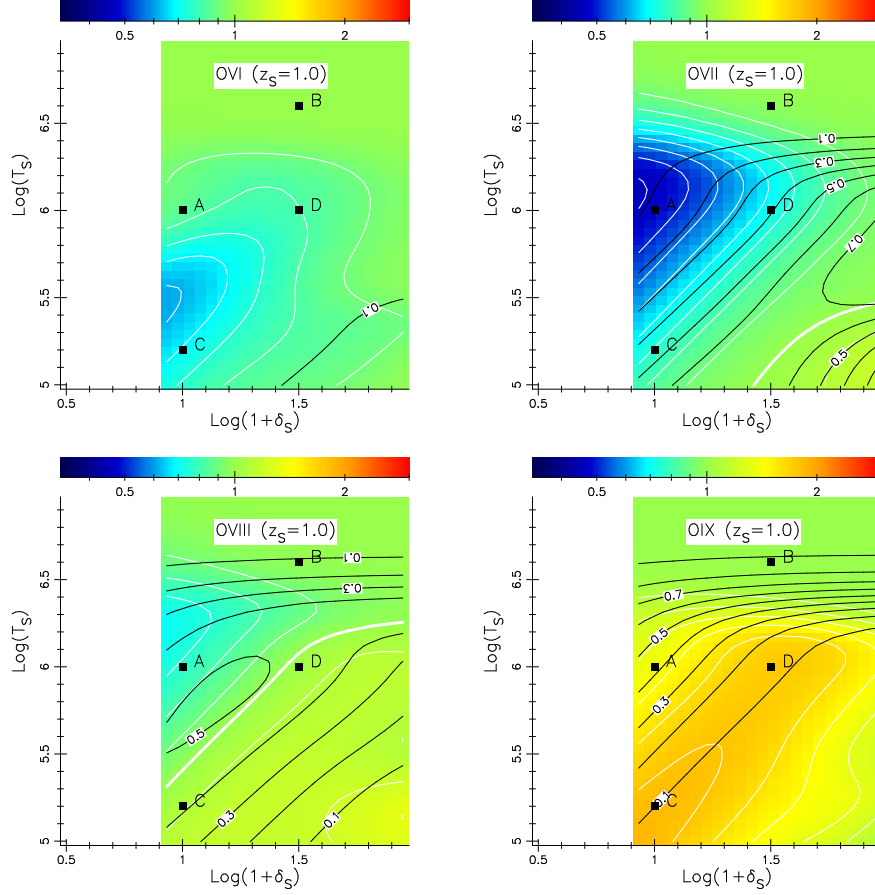


Fig. 6. Maps of ratios of ionization fractions between non-equilibrium and equilibrium ionization states for O VI, O VII, O VIII and O IX at redshift $z = 0$ on a $(1 + \delta_s)$ – T_s plane, where shock heating epoch is set to $z_s = 1.0$. White contours are separated by a factor of 1.1 in the ratios of the ionization fractions. Black lines with numeric labels are the contours of the ionization fractions in the ionization equilibrium states.

in the initial epoch. Thermal history of each gas particle is interpolated if an time interval between two continuous outputs is longer than the timestep Δt in integrating equation (5). The calculations are carried out with timesteps of 10^7 yr and 3×10^6 yr for a convergence test, and we verify that the results with two different timesteps are consistent with each other. Note that our methodology is not fully self-consistent because the thermal history of each gas particle, with which its non-equilibrium ionization state is calculated, is computed with the cooling rate in the collisional ionization equilibrium by Sutherland & Dopita (1993). However, since the cooling time for hot ($T \simeq 10^6$ K) and low density ($1 + \delta_b \simeq 1$) gas like WHIM is much longer than the hubble time, the effect of radiative cooling on its thermal history is rather mild, and such inconsistency in radiative cooling does not drastically change its thermal history. Therefore, we believe that our results presented in this paper is useful as a first approximation of non-equilibrium ionization state in WHIM.

Figure 10 depicts mean ratios of ionization fractions of O VI, O VII, O VIII and O IX in the

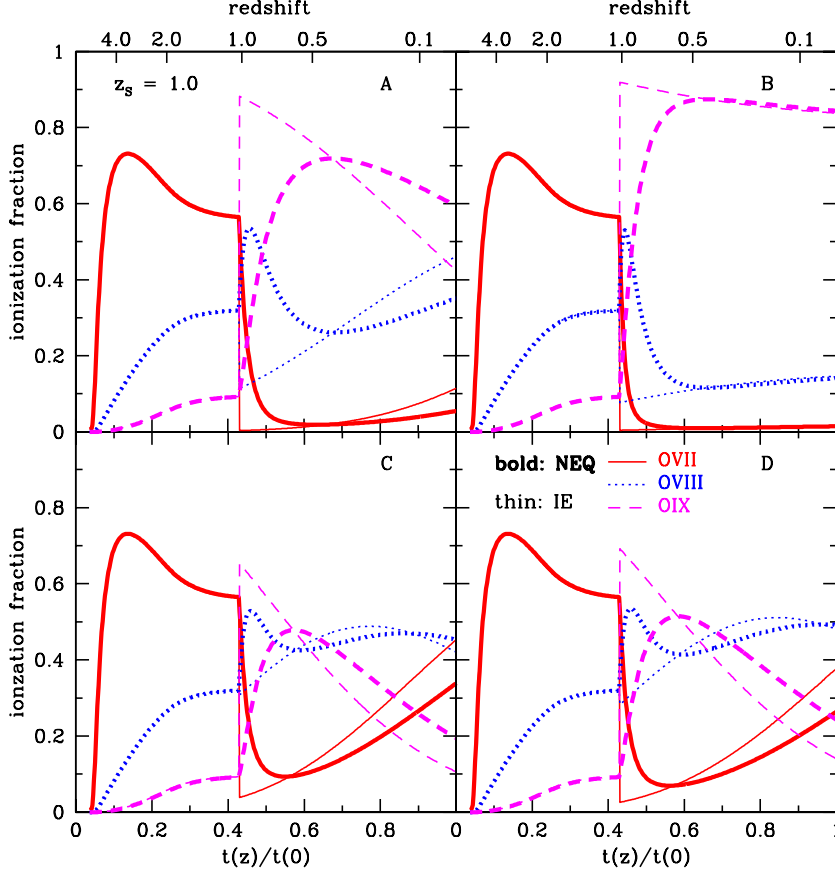


Fig. 7. Time evolution of ionization fractions of O VII, O VIII and O IX for four sets of the densities and temperatures at redshift $z = 0$ marked in figure 6. Bold and thin lines indicate the non-equilibrium and equilibrium states, respectively.

non-equilibrium state at $z = 0$ relative to those in the equilibrium state on a $(1 + \delta_b) - T$ plane, where δ_b is the baryon overdensity. Black contours in each panel indicate the mass distribution of the corresponding ion, and 25%, 50% and 75% of its mass are enclosed by three contour lines from inside to outside. One can see that most of O VI ions are close to their ionization equilibrium states, and that, the deviations of O VII, O VIII and O IX ions from the ionization equilibrium are not negligible. In addition, all of O VII, O VIII and O IX ions with $(1 + \delta_b) > 10^2$ and $T > 10^{6.5} \text{K}$ are close to the ionization equilibrium. These features are similar to the results for simple thermal histories described in the previous section, and can be understood by the same arguments on the timescales of ionization and recombination processes. It should be also noted that deviation from ionization equilibrium states at low density regimes with $1 + \delta_b \lesssim 10$ is quite similar to that in the simple models with $z_s = 0.1$ (see figure 9), indicating that the baryons in these low density regions recently experienced shock heating.

In figure 11, we show the spatial distribution of hydrogen number density and the ratios of O VI, O VII and O VIII fractions in the non-equilibrium state relative to those in the ionization

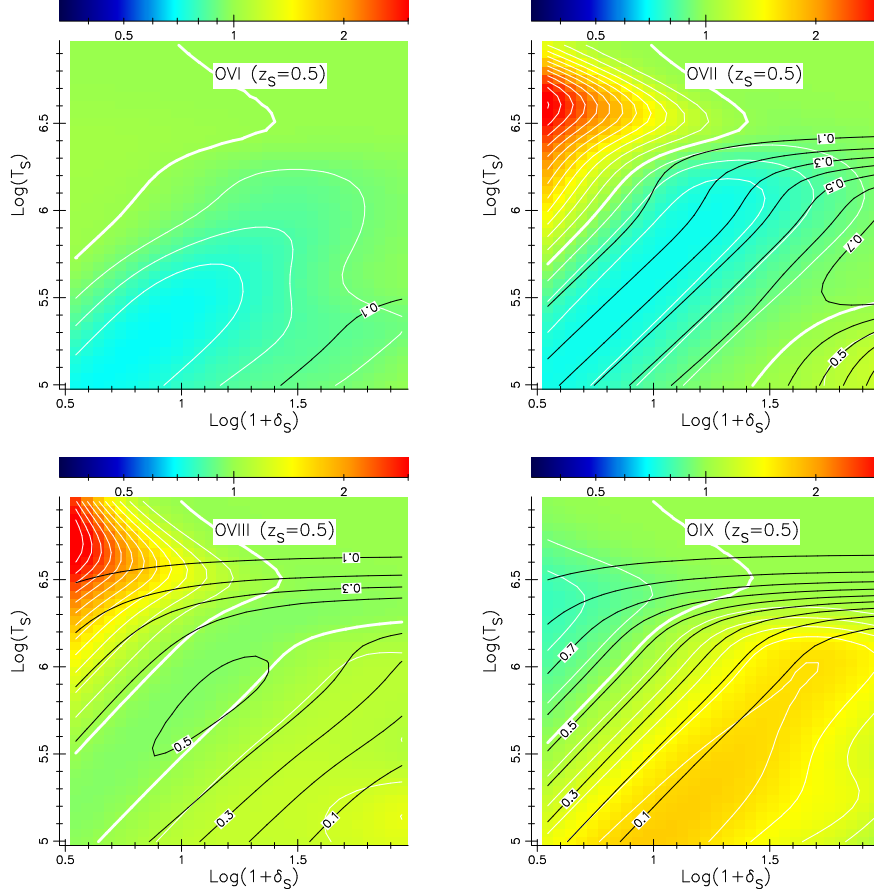


Fig. 8. Same as figure 6 except that shock heating epoch is set to $z_s = 0.5$.

equilibrium state in a $7.5h^{-1}$ thick slice taken from the simulation box at $z = 0$. In this slice, we have a galaxy cluster at $(X, Y) = (32, 25)h^{-1}$ Mpc, and a prominent filamentary structure associated with this galaxy cluster. A close look at figure 11 shows that we have significant deviation from the ionization equilibrium state at the outskirts of galaxy clusters and filamentary structures, where cosmological shocks occur (Kang et al. 2005).

5. EFFECT ON DETECTABILITY AND OBSERVABLES OF WHIM

The deviations of ionization fractions of O VI, O VII and O VIII from the ionization equilibrium state shown in the previous section will affect the observational features of WHIM. In this section, using the results obtained in the previous section, we present to what extent the detectability and observables of WHIM through its emission and absorption signatures are altered by relaxing the assumption of the ionization equilibrium. For a mock observation of WHIM, we construct a lightcone data up to a redshift of $z = 0.3$ by stacking 11 simulation cubes in the same way as described in Yoshikawa et al. (2003). The lightcone data has a $5^\circ \times 5^\circ$ field-of-view and contains the ionization fractions of ions for each gas particle computed in the previous section as well as those in the ionization equilibrium state.

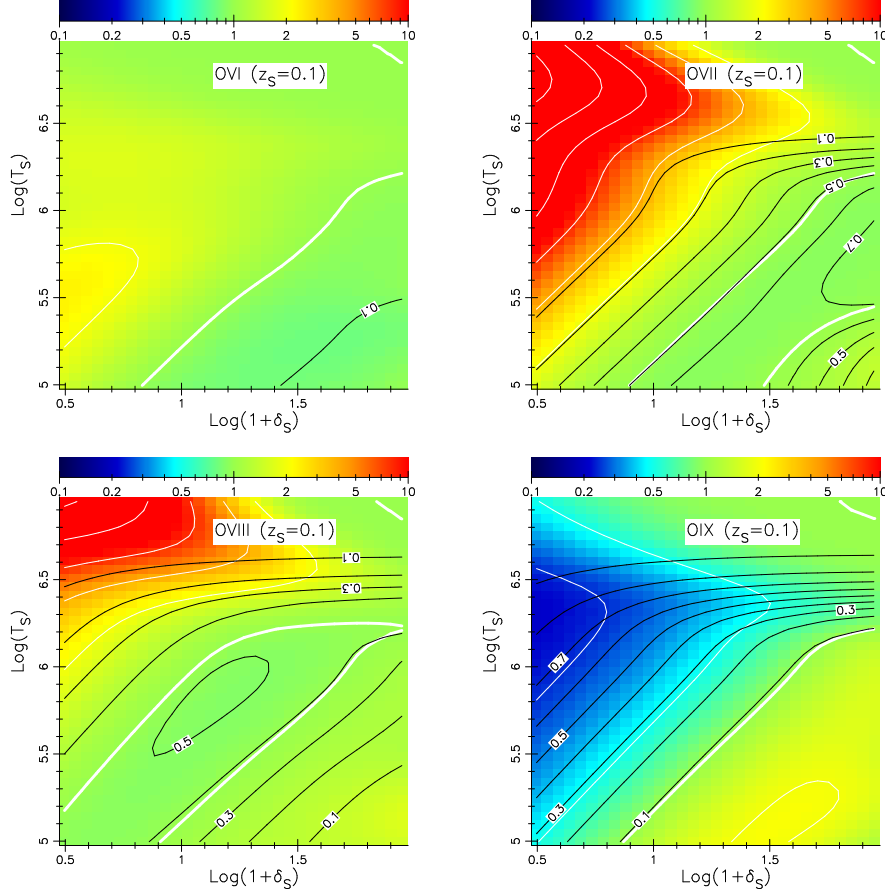


Fig. 9. Same as figure 6 except that shock heating epoch is set to $z_s = 0.1$. Note that the ranges of the ratios are different from those in figure 6 and 8.

5.1. Detection through emission

Surface brightness of emission lines of O VII at 574eV and O VIII at 653eV (S_{OVII} and S_{OVIII} , respectively) are computed for both of the equilibrium and non-equilibrium states. Here, we assume the latest specification of the detector proposed for *DIOS* mission (Ohashi et al. 2004), namely a spectroscopic energy resolution of 2 eV and a spatial resolution of 5 arcmin. Figure 12 depicts the ratios of surface brightness in the non-equilibrium state relative to that in the ionization equilibrium state $S_{\text{OVII}}/S_{\text{OVII}}^{\text{eq}}$ and $S_{\text{OVIII}}/S_{\text{OVIII}}^{\text{eq}}$, separately for line emitters at redshift ranges of $0.0 < z < 0.15$ (lower panels) and $0.15 < z < 0.3$ (upper panels). Vertical dotted lines in all the panels indicate the nominal detection limit of *DIOS* mission ($10^{-11} \text{ erg s}^{-1} \text{ cm}^{-2} \text{ sr}^{-1}$). Note that we have significant deviations of surface brightness ratios from unity at $\simeq 10^{-9} \text{ erg s}^{-1} \text{ cm}^{-2} \text{ sr}^{-1}$ in O VII emission and $\simeq 10^{-8} \text{ erg s}^{-1} \text{ cm}^{-2} \text{ sr}^{-1}$ in O VIII emission. It is found that these strong deviations take place at the very central regions of galaxy clusters and are caused by shocks inside them. One can see that surface brightness of O VIII (653 eV) emission lines in the non-equilibrium ionization state is quite close to that in the equilibrium state, and that O VII (574 eV) emissions are only slightly brighter than those

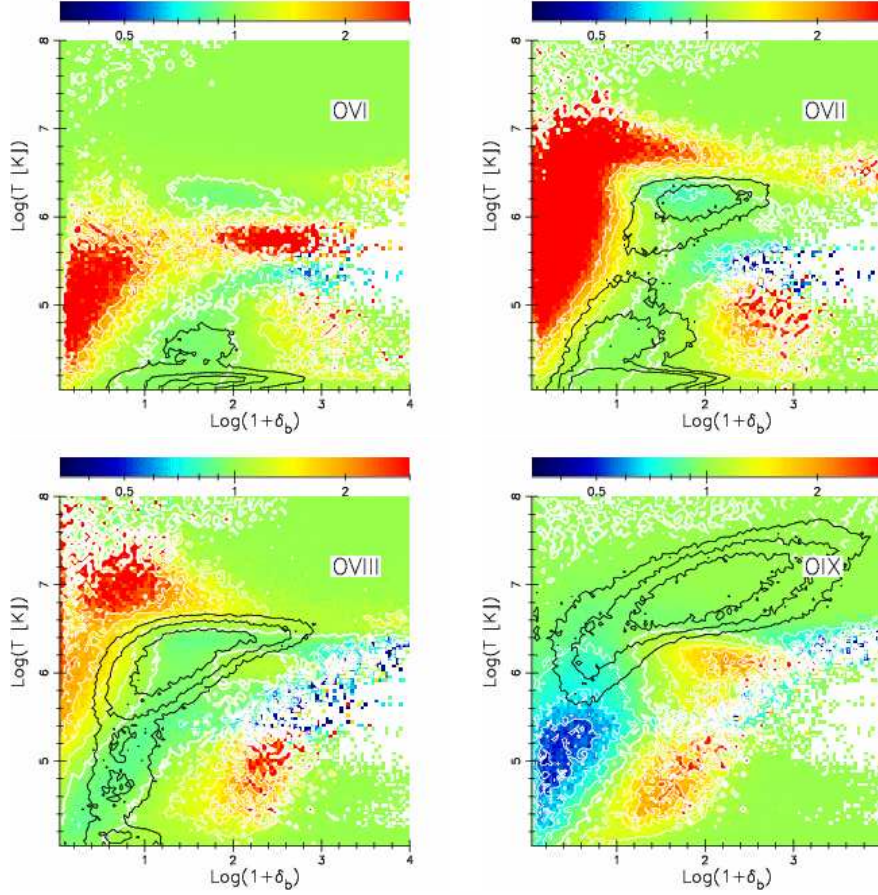


Fig. 10. Mean ratios of ionization fractions at $z = 0$ between non-equilibrium and equilibrium ionization states for O VI, O VII, O VIII and O IX on the $(1 + \delta_b)$ – T plane. White contours are drawn in the regions with $0.5 < f_j/f_j^{\text{eq}} < 2$ and separated by a factor of 1.2 in the ratios of ionization fractions. The white solid lines indicate the contour for $f_j/f_j^{\text{eq}} = 1$. Three black contours from inside to outside enclose the 25%, 50% and 75% of mass of each ionic species.

in the ionization equilibrium state above the detection limit of *DIOS* mission, irrespective of redshift of the line emitters. Therefore, the detectability of WHIM through its oxygen emission lines is not significantly different from the theoretical predictions based on the assumption of ionization equilibrium. Actually, the previous works on oxygen line emission of WHIM by Yoshikawa et al. (2003), Yoshikawa et al. (2004) and Fang et al. (2005) all assume the collisional ionization equilibrium. Therefore, it is useful to understand to what extent such an assumption is acceptable. Figure 13 shows the comparison of the surface brightness of O VII and O VIII emissions in the non-equilibrium state with those in the collisional ionization equilibrium, and indicate that the assumption of collisional ionization equilibrium is fairly valid for oxygen line emitters brighter than the nominal detection limit of *DIOS*, $10^{-11} \text{ erg s}^{-1} \text{ cm}^{-2} \text{ sr}^{-1}$. Therefore, the numerical predictions of detectability of WHIM through its oxygen line emission presented in Yoshikawa et al. (2003) and Yoshikawa et al. (2004) is not significantly altered by the effect of the non-equilibrium ionization balance.

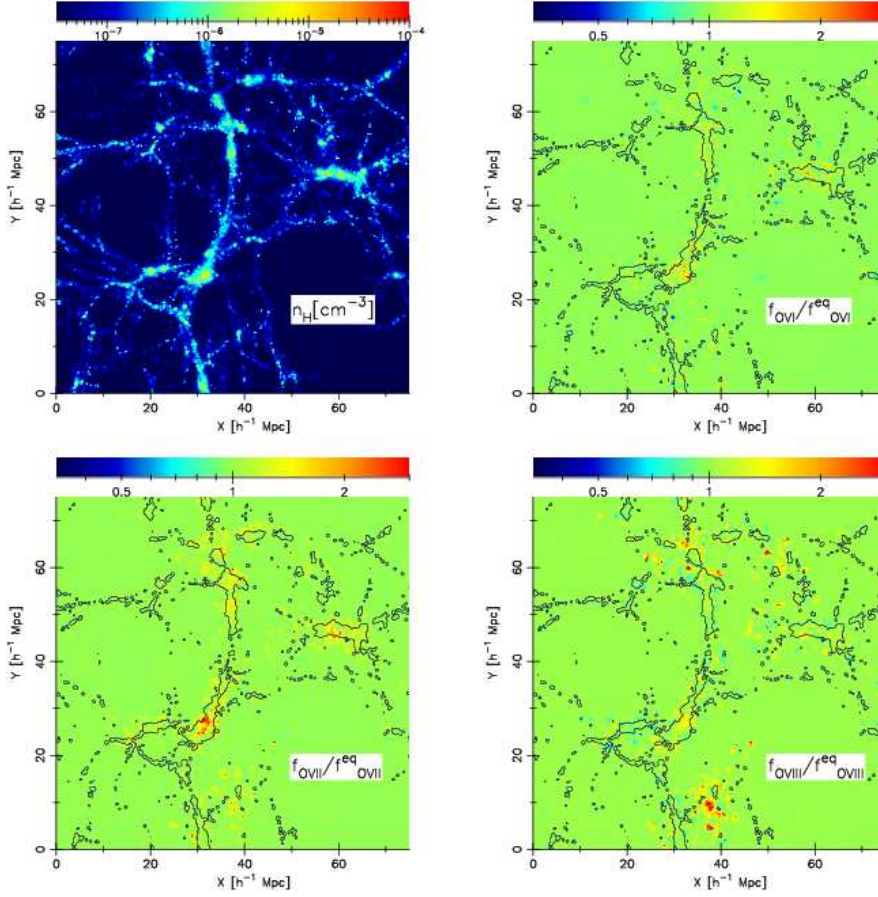


Fig. 11. Spatial distribution of hydrogen number density, and ratios of ionization fractions of O VI, O VII and O VIII between non-equilibrium and equilibrium states in the simulation volume at $z=0$. The thickness of the slice is $7.5h^{-1}\text{Mpc}$. Contours of baryon mass density for $1 + \delta_b = 1$ are also shown in the top-right, bottom-left and bottom right panels.

5.2. Detection through absorption

Column densities of O VI, O VII and O VIII (N_{OVI} , N_{OVII} , and N_{OVIII} , respectively) and those in ionization equilibrium ($N_{\text{OVI}}^{\text{eq}}$, $N_{\text{OVII}}^{\text{eq}}$ and $N_{\text{OVIII}}^{\text{eq}}$) are calculated for 10^4 randomly selected line-of-sights in the $5^\circ \times 5^\circ$ field-of-view by computing line integrals through the smoothing kernel of each gas particle, and individual absorbers are identified in the same way as done in Chen et al. (2003). Each line-of-sight is divided into $\simeq 16000$ bins along redshift direction. Thus, each bin has a width of $\simeq 5 \text{ km s}^{-1}$ in velocity units. Figure 14 shows the column density ratios of the identified absorbers in the non-equilibrium state relative to those in the ionization equilibrium state ($N_{\text{OVI}}/N_{\text{OVI}}^{\text{eq}}$, $N_{\text{OVII}}/N_{\text{OVII}}^{\text{eq}}$ and $N_{\text{OVIII}}/N_{\text{OVIII}}^{\text{eq}}$) as a function of the latter for absorbers at redshift ranges of $0.0 < z < 0.15$ (lower panels) and $0.15 < z < 0.3$ (upper panels) separately. As expected from the results shown in previous sections that most of O VI ions are quite close to the ionization equilibrium state, column densities of O VI absorbers are almost the same as those in the ionization equilibrium state, irrespective of the redshift of the

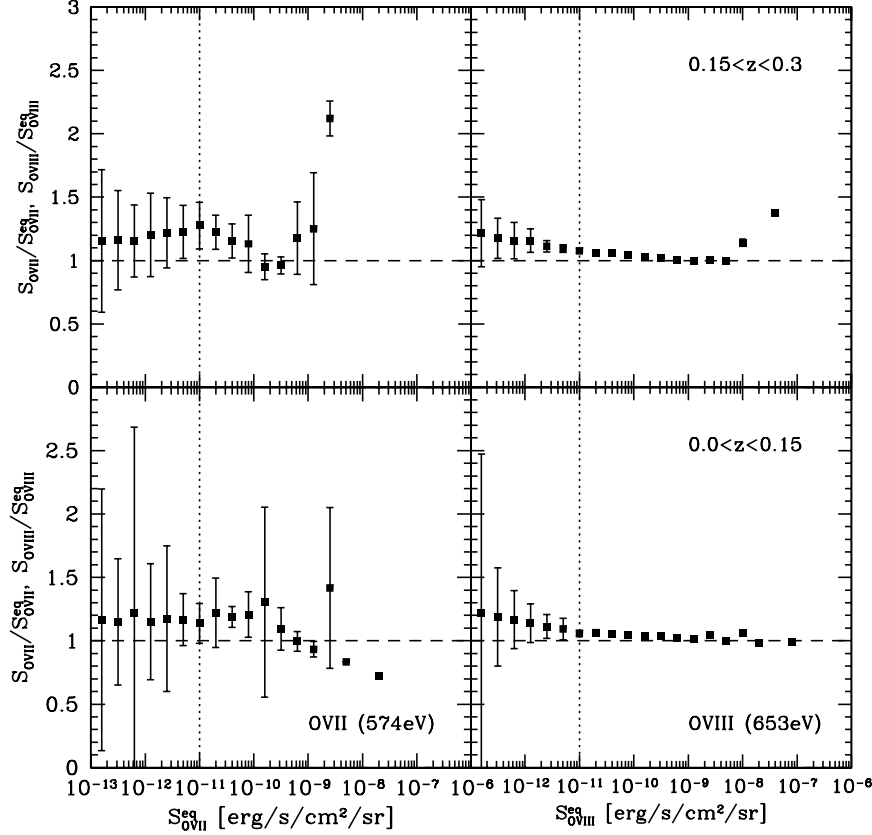


Fig. 12. Ratios of surface brightness of O VII (574eV) and O VIII (653eV) emission lines for non-equilibrium states relative to equilibrium states as a function of surface brightness in equilibrium states. Upper and lower panels are for line emissions at redshift ranges of $0.15 < z < 0.3$ and $0.0 < z < 0.15$, respectively. Symbols and error bars indicate the averages and the standard deviations for each horizontal bin. Vertical dotted lines in both panels indicate the nominal detection limit of *DIOS* mission.

absorbers. On the other hand, we have systematically larger O VII and O VIII column densities in the non-equilibrium ionization state and also have large statistical dispersions. However, the extent of difference in column densities between equilibrium and non-equilibrium states is so mild that the effect on detectability of WHIM through oxygen absorption lines is negligible.

5.3. Line Ratios

Apart from intensities of emission and absorption lines of WHIM, their ratios are also a very important observables as diagnostics for the nature of WHIM, in particular its temperature. Deviation from ionization equilibrium will cause difference in ratios of emission and absorption line intensities of WHIM from those with the assumption of ionization equilibrium, and uncertainty in estimation of temperature of WHIM.

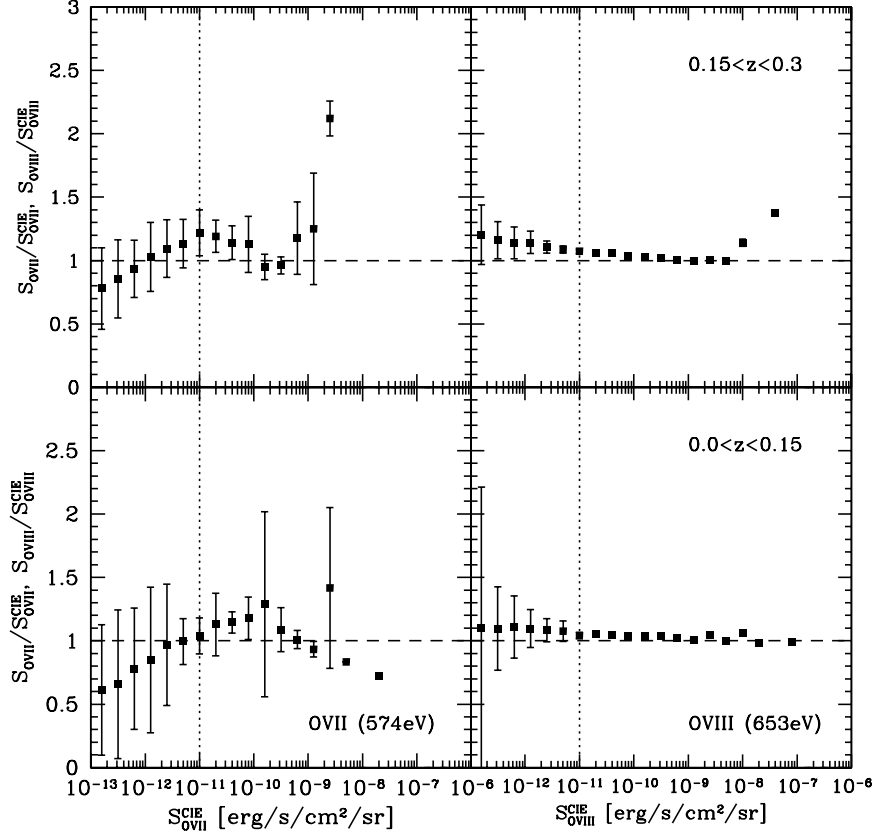


Fig. 13. Same as figure 12, except that ratios relative to surface brightness in the collisional ionization equilibrium state are shown.

Figure 15 depicts the relation of emission line ratios $S_{\text{O VIII}}/S_{\text{O VII}}$ between equilibrium and non-equilibrium states for line emitters at $0.0 < z < 0.15$ (left panels) and $0.15 < z < 0.3$ (right panels). Here, line emitters with either $S_{\text{O VII}}^{\text{eq}}$ or $S_{\text{O VIII}}^{\text{eq}}$ larger than $10^{-11} \text{ erg s}^{-1} \text{ cm}^{-2} \text{ sr}^{-1}$ are considered. One can see that the line ratios $S_{\text{O VIII}}/S_{\text{O VII}}$ in the non-equilibrium state are systematically lower than those in the ionization equilibrium state, especially at $S_{\text{O VIII}}/S_{\text{O VII}} \gtrsim 10$ for both redshift ranges. Actually, we find that line emitters with $S_{\text{O VIII}}$ or $S_{\text{O VII}} \simeq 10^{-11} \text{ erg s}^{-1} \text{ cm}^{-2} \text{ sr}^{-1}$ mainly contributes to these differences line ratios, and that line ratios of emitters whose $S_{\text{O VII}}$ and $S_{\text{O VIII}}$ exceed $10^{-10} \text{ erg s}^{-1} \text{ cm}^{-2} \text{ sr}^{-1}$ are statistically consistent with those in the ionization equilibrium state.

Relation between column density ratios $N_{\text{O VII}}/N_{\text{O VI}}$ and $N_{\text{O VIII}}/N_{\text{O VII}}$ in the ionization equilibrium and non-equilibrium states are shown in figure 16 for absorbers at redshift $0.0 < z < 0.15$ (left panel) and $0.15 < z < 0.3$ (right panel), separately. Here, column density ratios $N_{\text{O VII}}/N_{\text{O VI}}$ ($N_{\text{O VIII}}/N_{\text{O VII}}$) are considered for absorbers whose $N_{\text{O VI}}$ or $N_{\text{O VII}}$ ($N_{\text{O VIII}}$ or $N_{\text{O VII}}$)

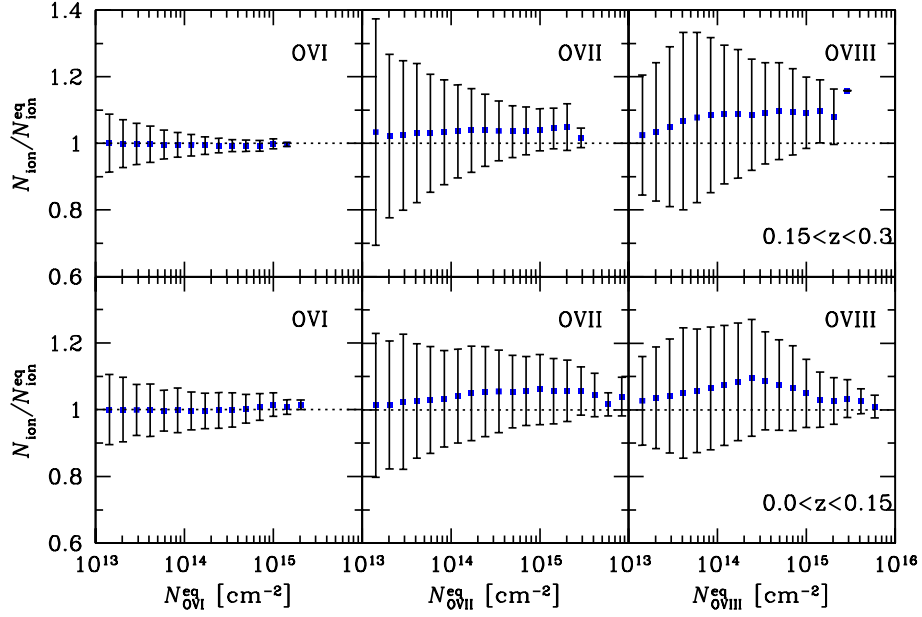


Fig. 14. Ratios of O VI, O VII and O VIII column densities of absorbers at redshift $0.0 < z < 0.15$ (lower panels) and $0.15 < z < 0.3$ (upper panels) in non-equilibrium states relative to those in ionization equilibrium states identified in the lightcone data as a function of column densities in ionization equilibrium states. Symbols and error bars indicate the averages and standard deviations for corresponding horizontal bins, respectively.

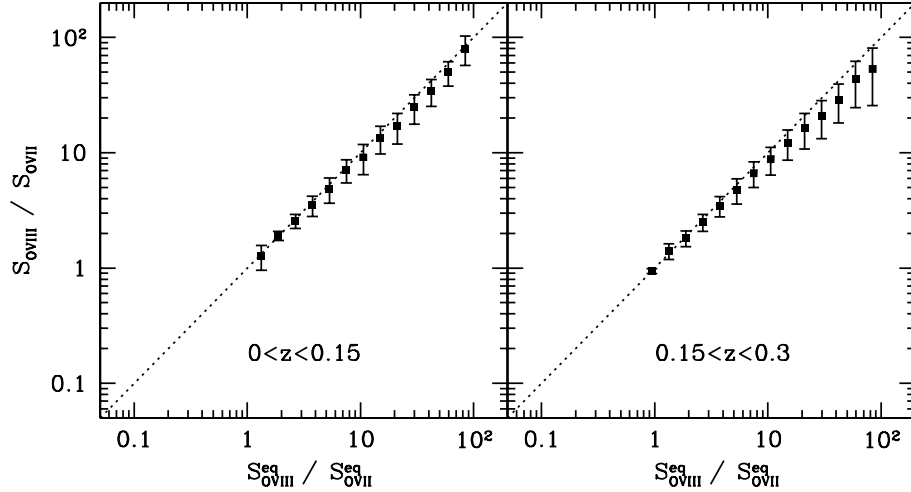


Fig. 15. Relations of line emission ratio $S_{\text{O VIII}}/S_{\text{O VII}}$ between non-equilibrium and equilibrium states. Symbols and error bars indicate the averages and standard deviations for corresponding horizontal bins, respectively.

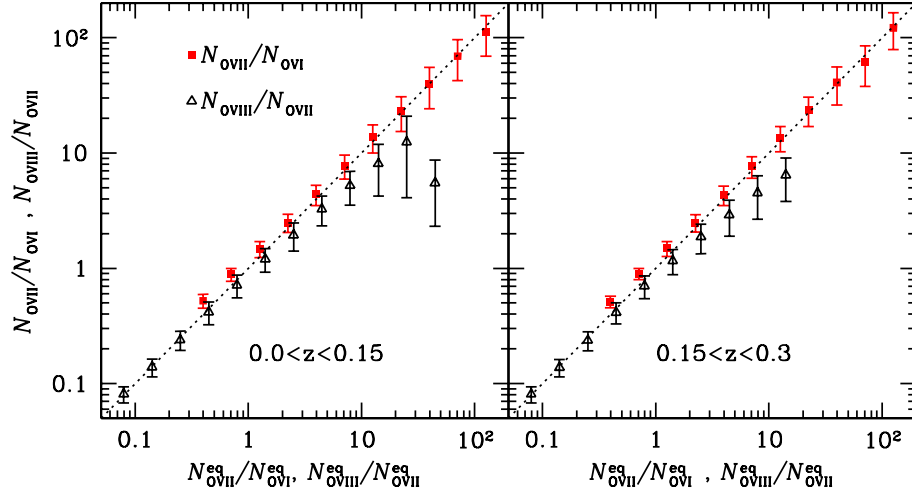


Fig. 16. Relations of column density ratios $N_{\text{O VII}}/N_{\text{O VI}}$ (filled squares) and $N_{\text{O VIII}}/N_{\text{O VII}}$ (open triangles) between non-equilibrium and equilibrium states. Symbols and error bars indicate the averages and standard deviations for corresponding horizontal bins, respectively.

exceed 10^{14} cm^{-2} . Although $N_{\text{O VII}}/N_{\text{O VI}}$ in the non-equilibrium state statistically agrees well with that in the ionization equilibrium state in both redshift ranges, the non-equilibrium state exhibits systematically lower $N_{\text{O VIII}}/N_{\text{O VII}}$ than the ionization equilibrium state. It is found that these differences in $N_{\text{O VIII}}/N_{\text{O VII}}$ are due to the absorbers with low ($\simeq 10^{14} \text{ cm}^{-2}$) column density of O VII and O VIII ions.

The location and the physical conditions where the line ratio between O VIII and O VII deviates from that in ionization equilibrium state are of great interest. Here we define the ratio of ionization fractions of O VIII relative to O VII in equilibrium and non-equilibrium state as

$$R \equiv \frac{f_{\text{O VIII}}}{f_{\text{O VII}}} \quad (6)$$

and

$$R^{\text{eq}} \equiv \frac{f_{\text{O VIII}}^{\text{eq}}}{f_{\text{O VII}}^{\text{eq}}}. \quad (7)$$

Note that $S_{\text{O VIII}}/S_{\text{O VII}}$ and $N_{\text{O VIII}}/N_{\text{O VII}}$ are roughly proportional to R . Figure 17 shows the map of R/R^{eq} at a redshift of $z = 0$ in the same slice of the simulation volume as figure 11, and indicates that we have $R/R^{\text{eq}} \lesssim 1$ ubiquitously in filamentary structures. This is why the line ratios, $S_{\text{O VIII}}/S_{\text{O VII}}$ and $N_{\text{O VIII}}/N_{\text{O VII}}$, are systematically smaller than those in the ionization equilibrium state. The left panel of figure 18 shows the contour map of R/R^{eq} on a $(1 + \delta_b)$ - T plane, on which three contours for $R^{\text{eq}} = 0.1, 1$ and 10 are overlaid from bottom to top. Considering the fact that the $S_{\text{O VIII}}/S_{\text{O VII}}$ and $N_{\text{O VIII}}/N_{\text{O VII}}$ in the non-equilibrium ionization state are lower than their equilibrium values at $S_{\text{O VIII}}^{\text{eq}}/S_{\text{O VII}}^{\text{eq}} \gtrsim 10$ and $N_{\text{O VIII}}^{\text{eq}}/N_{\text{O VII}}^{\text{eq}} \gtrsim 10$, respectively, the left panel of figure 18 indicates that the regions responsible for such departures

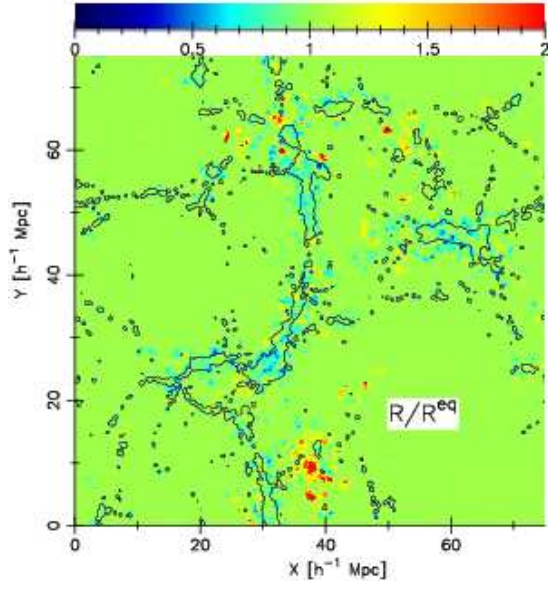


Fig. 17. Spatial distribution of R/R^{eq} at $z=0$ in the same slice of the simulation volume as in figure 11. Contours for baryon mass density of $1 + \delta_b = 1$ are also shown.

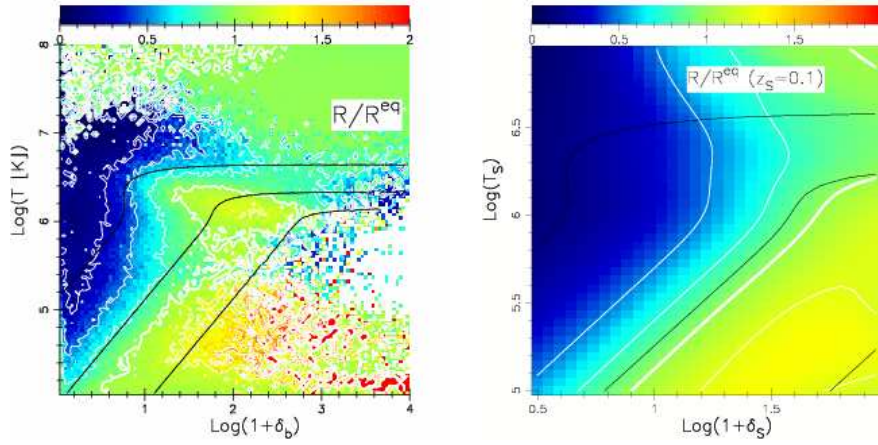


Fig. 18. Maps of R/R^{eq} at $z=0$ on a $(1 + \delta_b)$ - T plane in a numerical simulation (left panel) and in a simple model with $z_s = 0.1$ (right panel). White contours are separated by a difference of 0.25 in R/R^{eq} and bold lines indicate $R/R^{\text{eq}} = 1$. Three black contours in each panel are for $R^{\text{eq}} = 0.1, 1$ and 10 from bottom to top.

in line ratios from the equilibrium state have a typical density of $1 + \delta_b \simeq 10$ and temperature of $T \simeq 10^{6-7} \text{K}$. The right panel of figure 18 is the map of R/R^{eq} at $z = 0$ in the simple model with $z_s = 0.1$ described in section 3, and shows the essentially same behavior of R/R^{eq} on the $(1 + \delta_b) - T$ plane. This suggests that the regions with $R/R^{\text{eq}} < 1$ experienced a shock heating very recently around a redshift of $z \simeq 0.1$, and that over abundant O VII ions due to the non-negligible timescale for the ionization from O VII to O VIII reduces R/R^{eq} to below unity. Note that the loci with $R/R^{\text{eq}} < 1$ on the $(1 + \delta_b) - T$ plane in figure 18 and those with $f_{\text{OVII}}/f_{\text{OVII}}^{\text{eq}} > 1$ roughly coincide (see upper right panels of figure 9 and 10).

6. CONCLUSION AND DISCUSSION

We investigate the non-equilibrium ionization state of oxygen ions in WHIM by relaxing the assumption of ionization equilibrium and directly integrating the time evolution of their ionization fractions along the cosmological thermal histories of the baryons.

First, we consider the general features of the non-equilibrium ionization state for simple models of thermal histories of the cosmic baryons, and find that ionization states of O VII, O VIII and O IX ions are significantly different from those in the ionization equilibrium state especially in typical physical conditions for WHIM, while most of O VI ion are close to the ionization equilibrium state. These deviations from the ionization equilibrium are caused by the fact that timescales for ionization and recombination processes of these ions are comparable to or even longer than the hubble time in low density plasma like WHIM. Furthermore, we find that rapid decrease of the intensity of the UV and X-ray background radiation at redshift $z < 2$ also enlarge the deviation from the ionization equilibrium state. This is because the timescale of the recombination processes is so long that the recombination processes cannot catch up with the ionization equilibrium state, in which ionization fractions also vary with time as the UV and X-ray background radiation decays.

The evolution of ionization fractions of oxygen ions for thermal histories obtained in a cosmological hydrodynamic simulation is also investigated. The ionization state of oxygen ions at redshift of $z = 0$ is similar to that obtained in the simple models of thermal histories in which cosmological shocks take place at relatively recent epoch, say $z \lesssim 0.5$. Statistically, O VII and O VIII ions are over-abundant compared with the ionization equilibrium state in typical physical conditions for WHIM, while O VI ions are nearly in the ionization equilibrium state. Spatial distribution of the oxygen ions reveals that the deviations of ionization fractions of O VII and O VIII ions from the ionization equilibrium state take place at the outskirts of galaxy clusters and the edge of filamentary structures.

We also investigate the effect of such deviations of oxygen ions from the ionization equilibrium state on the detectability and observables of WHIM through its emission and absorption line features. It is found that although the surface brightness and column density of oxygen emission and absorption lines slightly differ from those in the ionization equilibrium state, the

overall detectability of WHIM is almost the same as what we have under the assumption of the ionization equilibrium. However, the ratios of emission and absorption line intensities between O VII and O VIII, which are considered to be important probes of temperature of WHIM, are significantly different from those in the ionization equilibrium. This means that the observed line ratios of WHIM may not reflect its real temperature. It is found that the regions where the line ratios are different from those in the ionization equilibrium are located at outer edges of filamentary structures. Distribution of such regions on a density–temperature plane is similar to the result of the simple model for the cosmological thermal history with $z_s = 0.1$ described in section 3. These facts indicate that recent cosmological shocks near the edge of filaments around a redshift of $z \simeq 0.1$ cause the departure of line ratios from the ionization equilibrium state.

In this paper, several important physical processes are missed. First of all, in our simulation, the effects of energy feedback and metal ejection from galaxies are ignored, and we assume that the metallicity of the cosmic baryons is spatially uniform and constant irrespective of redshift. Since oxygen atoms are mainly supplied by type-II supernovae followed by the formation of massive stars, the spatial distribution of oxygen is obviously time dependent and inhomogeneous. Furthermore, the energy feedback by supernova explosions will affect the thermal history of intergalactic medium (or WHIM) in the vicinity of galaxies. Therefore, a self-consistent treatment of galaxy formation and its feedback effect is required for better understanding of the non-equilibrium ionization state of ions in WHIM. Recently, Cen & Ostriker (2006) and Cen & Fang (2006) performed numerical simulations in which the non-equilibrium ionization state of oxygen ions is considered together with energy feedback and metal pollution caused by galaxy formation. According to their results, energy feedback induces strong shocks and additional non-equilibrium ionization state in the intergalactic medium around galaxies if the energy feedback is strong enough as performed in their simulations. Therefore, the deviation from ionization equilibrium of oxygen ions in WHIM presented in this paper can be regarded as its lower limit, and the actual deviations from the ionization equilibrium may be much larger.

Secondly, it is assumed that equipartition between electrons and ions is achieved instantaneously, or, in other words, electrons and ions always have a locally common temperature. At cosmological shocks, by which most of WHIM is heated, nearly all of the kinetic energy is converted into the thermal energy of ions just after the shock. Actually, collisional relaxation between ions and electrons through coulomb scattering takes a long time which is comparable to the hubble time in a low density plasma like WHIM. Therefore, as numerically shown by Takizawa (1998) and Yoshida, Furlanetto, & Hernquist (2005), the electron temperature T_e can be systematically lower than the ion temperature T_i by a factor of a few in the outskirts of galaxy clusters and WHIM, unless other physical processes which convert the bulk kinetic energy into electron thermal energy (e.g., Laming 2000) work efficiently. Since the ionization and recombination rates $S_{i,j}$ and α_j in equation (1) depend on the electron temperature T_e

rather than the ion temperature T_i , such difference between T_i and T_e will affect the results obtained in this paper. We will address this issue in near future by considering the relaxation processes between ions and electrons.

We would like to thank an anonymous referee for his/her useful comments and suggestions. Numerical computations presented in this paper were carried out at the Astronomical Data Analysis Center of the National Astronomical Observatory of Japan (project ID: wky17b). KY acknowledge support from the Japan Society for the Promotion of Science.

References

- Anninos, P., Zhang, Y., Abel, T., Norman, M.L. 1997, *NewA*, 2, 209
- Arnaud, M., & Rothenflug, R. 1985, *A&AS*, 60, 425
- Cen, R., & Ostriker, J.P. 1999, *ApJ*, 514, 1
- Cen, R., Tripp, T.M., Ostriker, J.P., Jenkins, E.B. 2001, *ApJ*, 559, 5
- Cen, R., Ostriker, J.P. 2006, *ApJ* submitted (astro-ph/0601008)
- Cen, R., Fang, T. 2006, *ApJ* submitted (astro-ph/0601009)
- Chen, X., Weinberg, D.H., Katz, N., & Davé, R. 2003, *ApJ*, 594, 42
- Davé, R., Cen, R., Ostriker, J.P., Bryan, G.L., Hernquist, L., Katz, N., Weinberg, D.H., Norman, M.L., & O’Shea, B. 2001, *ApJ*, 552, 473
- Elvis, M. S., & Fiore, F. 2003, *Proc. SPIE*, 4851, 377
- Elvis, M., Nicastro, F., & Fiore, F. 2004, 35th COSPAR Scientific Assembly, 563
- Fang, T., & Canizares, C.R. 2000, *ApJ*, 532, 539
- Fang, T., & Bryan, G.L. 2001, *ApJ*, 561, L31
- Fang, T., Marshall, H.L., Lee, J.C., Davis, D.S. & Canizares, R. 2002, *ApJ*, 572, L127
- Fang, T., Croft, R. A. C., Sanders, W. T., Houck, J., Davé, R., Katz, N., Weinberg, D. H., & Hernquist, L. 2005, *ApJ*, 623, 612
- Finoguenov, A., Briel, U.G., Henry, J.P. 2003, *A&A*, 410, 777
- Fujimoto, R., Takei, Y., Tamura, T., Mitsuda, K., Yamasaki, N.Y., Shibata, R., Ohashi, T., Ota, N., Audley, M.D., Kelley, R.L., Kilbourne, C.A. 2004, *PASJ*, 56, 29
- Fukugita, M., Hogan, C.J., & Peebles, P.J.E. 1998, *ApJ*, 503, 518
- Haardt, F., & Madau, P. 2001, in *Proceedings of the XXXVIth Rencontres de Moriond*, eds. D.M. Neumann et al. (astro-ph/0106018)
- Hellsten, U., Gnedin, N.Y., & Miralda-Escude, J. 1998, *ApJ*, 509, 56
- Kang, H., Ryu, D., Cen, R., & Song, D. 2005, *ApJ*, 620, 21
- Kaastra, J.S., & Jansen, F.A. 1993, *A&AS*, 97, 873
- Kaastra, J.S., Lieu, R., Tamura, T., Paerels, F.B.S., den Herder, J.W. 2003, *A&A*, 397, 445
- Kawahara, H., Yoshikawa, K., Sasaki, S., Suto, Y., Kawai, N., Mitsuda, K., Ohashi, T., & Yamasaki, N. 2005, submitted to *PASJ*, (astro-ph/0504594)
- Laming, J.M. 2000, *ApJS*, 127, 409
- Mathur, S., Weinberg, D.H., & Chen, X. 2003, *ApJ*, 582, 82

- Miyaji, T., Ishisaki, Y., Ogasaka, Y., Ueda, Y., Freyberg, M.J., Hasinger, G., & Tanaka, Y. 1998, A&A, 334, L13
- Nicastro, F., et al. 2002, ApJ, 573, 157
- Nicastro, F., et al. 2005, Nature, 433, 495
- Nicastro, F., et al. 2005, ApJ, 629, 700
- Ohashi, T., et al. astro-ph/0402546
- Perna, R., & Loeb, A. 1998, 503, L135
- Shull, J.M., Roberts, D., Giroux, M.L., Penton, S.V., & Fardal, M.A. 1999, AJ, 118, 1450
- Sutherland, R.S., & Dopita, M. 1993, ApJS, 88, 253
- Takizawa, M. 1998, ApJ, 509, 579
- Tripp, T.M., Giroux, M.L., Stocke, J.T., Tumlinson, J., & Oegerle, W.R. 2001, ApJ, 563, 724
- Tripp, T.M., Savage, B.D., & Jenkins, E.B. 2000, ApJ, 534, L1
- Yoshida, N., Furlanetto, S.R., & Hernquist, L. 2005, ApJ, 618, 91
- Yoshikawa, K., Taruya, A., Jing, Y.P., & Suto, Y. 2001, ApJ, 558, 520
- Yoshikawa, K., Yamasaki, N.Y., Suto, Y., Ohashi, T., Mitsuda, K., Tawara, Y., & Furuzawa, A. 2003, PASJ, 55, 879
- Yoshikawa, K. et al., 2004, PASJ, 56, 939